EDGE ARTICLE

Dynamic-dependent selectivity in a bisphosphine iron spin crossover C–H insertion/π-coordination reaction†

Michael T. Davenport, [ID] Justin K. Kirkland and Daniel H. Ess [ID] *

Reaction pathway selectivity is generally controlled by competitive transition states. Organometallic reactions are complicated by the possibility that electronic spin state changes rather than transition states can control the relative rates of pathways, which can be modeled as minimum energy crossing points (MECPs). Here we show that in the reaction between bisphosphine Fe and ethylene involving spin state crossover (singlet and triplet spin states) that neither transition states nor MECPs model pathway selectivity consistent with experiment. Instead, single spin state and mixed spin state quasiclassical trajectories demonstrate nonstatistical intermediates and that C–H insertion *versus* π-coordination pathway selectivity is determined by the dynamic motion during reactive collisions. This example of dynamic-dependent product outcome provides a new selectivity model for organometallic reactions with spin crossover.

Introduction

Reaction pathway selectivity is generally evaluated using density functional theory (DFT) calculated potential energy surfaces combined with transition-state theory or related statistical theories.[1–3] For many organometallic systems, an additional complication to evaluating pathway selectivity arises for reactions with spin state crossover (*e.g.* singlet spin state to triplet spin state).[4,5] In these pathways, in addition to calculating transition states and intermediates it is common to locate so-called minimum energy crossing point (MECP) structures where two spin states have identical structures and energies.[6] While not a stationary point, a MECP represents a portion of the potential energy surface where there is high probability of spin crossover and, like a transition state, MECPs have the potential to be a reaction pathway bottleneck and control selectivity.

An example of a reaction where spin crossover potentially impacts pathway selectivity was reported by Field where singlet spin $(DEPE)_2Fe(CH_3)(H)$ (DEPE = 1,2-bis(diethylphosphino) ethane) undergoes reductive elimination of methane to generate the triplet spin $(DEPE)_2Fe$ intermediate followed by reaction with ethylene to give a kinetic 95 : 5 ratio of the singlet vinyl C–H insertion $(DEPE)_2Fe(H)(C_2H_3)$ complex **I** and the singlet π-coordination $(DEPE)_2Fe(\eta^2-C_2H_4)$ complex **II** (Fig. 1a).[7,8] This reaction is a unique example where the π-coordination structure **II** is thermodynamically more stable and does not convert to the Fe-vinyl hydride **I**.[9] We initially assumed

that the location of singlet and triplet spin transition-state structures and MECPs would provide a qualitative (and quantitative) model for $(DEPE)_2Fe$–ethylene vinyl C–H insertion *versus* π-coordination selectivity.[10] In this type of statistical-based selectivity model, like transition-state theory, the $(DEPE)_2Fe$ intermediate would have separate transition states or MECPs that each provide a competitive kinetic bottleneck for forming **I** and **II** where the energy difference between these bottlenecks would translate to the product ratio. This type of general selectivity model with MECPs is outlined in Fig. 1b. Surprisingly, however, using transition states and MECPs for the statistical evaluation of reaction pathway selectivity gives selectivity opposite to experiment. This prompted us to perform single spin state and mixed spin state quasiclassical direct dynamics trajectories for reactive collisions between the bisphosphine Fe complex and ethylene, which provides a nonstatistical evaluation of reaction selectivity.[11,12] The DFT direct dynamics trajectories revealed that dynamic motion during the collision between the reactive bisphosphine Fe complex and ethylene controls C–H insertion *versus* π-coordination selectivity. Fig. 1c outlines this dynamic motion model with qualitative trajectories leading **I** and **II** and overlaid singlet and triplet energy surfaces. The discovery of nonstatistical dynamic selectivity[12–16] provides a new framework for modeling product outcomes in organometallic spin crossover reactions.

Results and discussion

Energy surfaces and statistical theory based analysis

Field reported that the reaction between $(DEPE)_2Fe(CH_3)(H)$ and ethylene after ~6 hours at −28 °C results in a 95 : 5 kinetic mixture of the C–H insertion product $(DEPE)_2Fe(H)(C_2H_3)$ **I** to

Department of Chemistry and Biochemistry, Brigham Young University, Provo, Utah, USA 84604. E-mail: dhe@chem.byu.edu

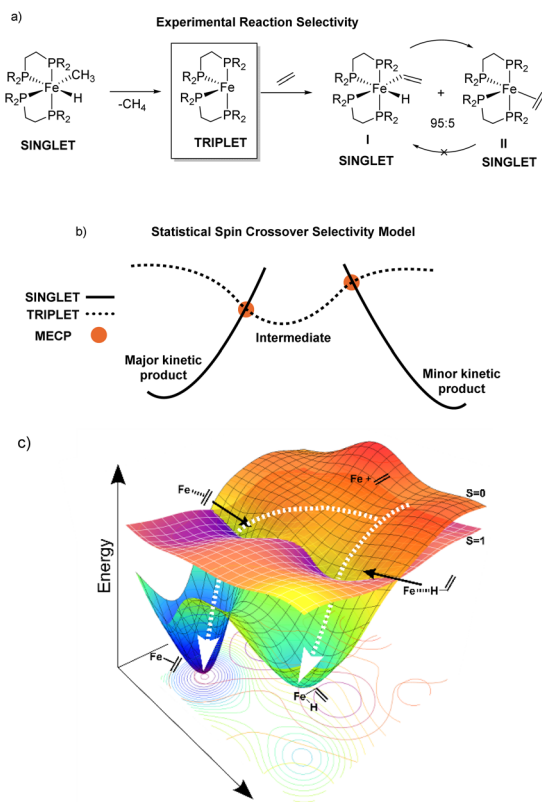**Fig. 1** (a) Outline of the spin crossover reaction for reductive elimination of methane from $(DEPE)_2Fe(CH_3)(H)$ followed by reaction of triplet spin intermediate $(DEPE)_2Fe$ with ethylene leading to a kinetic product mixture of singlet $(DEPE)_2Fe(H)(C_2H_3)$ **I** and singlet $(DEPE)_2$-$Fe(\eta^2-C_2H_4)$ **II**. (b) Outline of a statistical-based selectivity model involving transition state or MECP kinetic bottlenecks. In this model the relative energies of the MECPs and/or transition states from the common intermediate determine selectivity. (c) Conceptual depiction of the overlay of singlet and triplet spin energy surfaces for reactive collision between the bisphosphine Fe complex intermediate and ethylene. Dynamics trajectories are represented by white dotted arrows.

the π-coordination product $Fe(DMPE)_2(\eta^2$-ethylene) **II**. When the temperature was increased to 25 °C **I** isomerized to **II** and it remained the only product. This indicates that the vinyl insertion product **I** is the kinetic product and the η^2-ethylene complex **II** is the thermodynamic product. As mentioned in the Introduction, this is a unique example where the π-coordination structure **II** is thermodynamically more stable and does not convert to the Fe-vinyl hydride **I**. This implies that in this reaction, and perhaps in other related reactions, π-coordination is not required to activate/cleave sp^2 C–H bonds.

Using unrestricted M06-L/Def2-TZVP//M06-L/6-31G** [LANL2DZ for Fe] (Gaussian 16)[17–20] we extensively explored the singlet and triplet spin state potential-energy surfaces with the ligand only slightly modified to be DMPE (1,2-bis(dimethylphosphino)ethane). The M06-L functional was selected because it provides accurate geometries and relative energies of spin states for first-row transition metals, especially Fe.[21,22] Calculations included the implicit solvent model for mesitylene.[23] As

anticipated, $(DMPE)_2Fe$ has a ground triplet spin state with the unrestricted, open-shell singlet 10.0 kcal mol^{-1} higher in energy (singlet has $\langle S^2 \rangle = 1.0$) on the electronic energy surface. Using our MECPro program,[24] we located the singlet–triplet MECP for $(DMPE)_2Fe$ (**MECP1**), which has an energy of 11.2 kcal mol^{-1} relative to the triplet structure. Importantly, the Fe-solvent structure $(DMPE)_2Fe(mesitylene)$ is endergonic by 1.7 kcal mol^{-1} relative to separated $(DMPE)_2Fe$ and mesitylene (see ESI†) and therefore, if the transient Fe-solvent intermediate is formed, it would be in equilibrium with the coordinatively unsaturated intermediate $(DMPE)_2Fe$ and unlikely to significantly affect the reaction with ethylene.

On the singlet spin state surface (Fig. 2, black surface), there is a σ-CH coordination structure **INT 2** that is stabilized by -3.9 kcal mol^{-1} relative to separated triplet $(DMPE)_2Fe$ and ethylene. This weak coordination intermediate leads to the C–H insertion transition state **TS 1** that results in the cis Fe-vinyl hydride product $(DMPE)_2Fe(H)(C_2H_3)$ **I**. Manual displacement of the **TS 1** negative vibrational mode followed by optimization provided assignment of **TS 1** to connect intermediate **INT 2** and product **I**. The C–H activation/hydrogen atom transfer transition state for reaction with *trans*-$(DMPE)_2Fe$ and ethylene is nearly 30 kcal mol^{-1} and not viable (see ESI†). This means that the equilibrium between *cis* and *trans* **I** occurs after kinetic formation of *cis* **I**. Consistent with experiment, the energy difference between *cis* and *trans* **I** is only 0.5 kcal mol^{-1} (see ESI†). No potential energy barrier was found for forming $(DMPE)_2Fe(\eta^2-C_2H_4)$ **II** starting from the *cis*-bisphosphine Fe complex (see ESI† for potential-energy scans). No stable π-coordination structure was found between the *trans*-bisphosphine Fe complex and ethylene. The π-coordination energy of ethylene is -33.9 kcal mol^{-1} relative to triplet $(DMPE)_2Fe$ and ethylene. Our calculations confirm that **II** is thermodynamically 15.8 kcal mol^{-1} more stable than **I**.

On the triplet surface (Fig. 2, blue surface) we located corresponding structures to those shown on the singlet surface. As expected, the triplet spin structures are much less stabilized and exhibit less coordination between the Fe metal center and the bisphosphine ligand to weaken the ligand field. For example, the triplet **I′** and **II′** complexes show elongated Fe–P bonds, and the triplet π-complex **INT 3′** has significantly longer coordination lengths. Fig. 3 displays 3D structures of the key stationary points and MECPs. Location of the π-coordination transition state, **TS 2′**, on the triplet surface indicates that this transition-state structure does not exist on the singlet surface due to the much more reactive singlet $(DMPE)_2Fe$ structure. The barrier for C–H bond cleavage on the triplet surface is >30 kcal mol^{-1} and is not competitive with the barrier for singlet spin C–H insertion.

Because the coordinatively unsaturated *cis*-$(DMPE)_2Fe$ complex has a triplet spin state and the insertion and π-coordination products have singlet spin states, there is the possibility of spin crossover resulting from collision with ethylene. Therefore, we extensively examined possible MECPs with ethylene in or near the coordination sphere of the Fe center. Fig. 2 shows the locations of **MECP2** and **MECP3**. **MECP2** with an energy of 5.9 kcal mol^{-1} connects the singlet and triplet
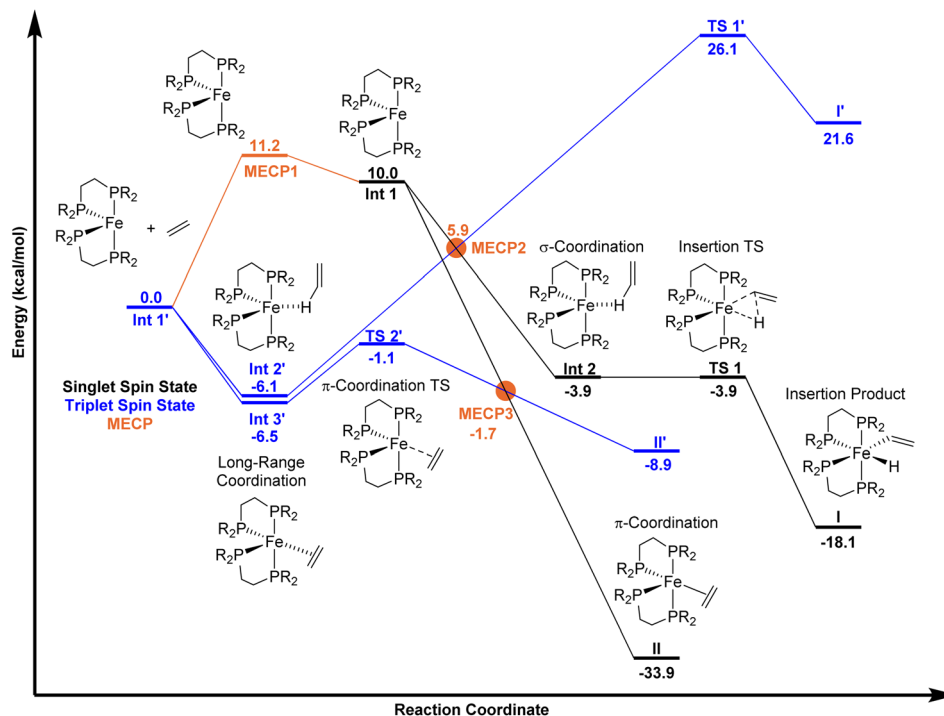
Fig. 2 M06-L potential energy landscapes for reaction between (DMPE)$_2$Fe and ethylene. Black numbers and lines represent unrestricted singlet spin-state energies. Blue numbers and lines represent unrestricted triplet spin-state energies. Orange dots give MECP energies. Energies are reported in kcal mol^{-1} (R = Me).

energy surfaces for the σ-CH coordination structure **INT 2'** and would precede **TS 1** for C–H bond cleavage. **MECP3** has a structure that likely provides singlet-triplet surface crossover for π-coordination to **II**.

The compilation of the singlet surface, the triplet surface, and the MECPs provides the possibility to estimate vinyl C–H insertion *versus* π-coordination selectivity using a statistical transition-state theory type approach. As described in the

Introduction, the slow step in the C–H insertion and/or π-coordination pathways can either be potential energy surface transition-state structures or MECP structures. Fig. 2 indicates that the lowest energy route to the C–H insertion product **I** involves first formation of the triplet π-complex **INT 3'** that is in equilibrium with the triplet σ-complex **INT 2'**. From **INT 2'**, spin crossover occurs through **MECP2** to generate the singlet σ-complex **INT 2** and then **TS 1** results in C–H insertion and the
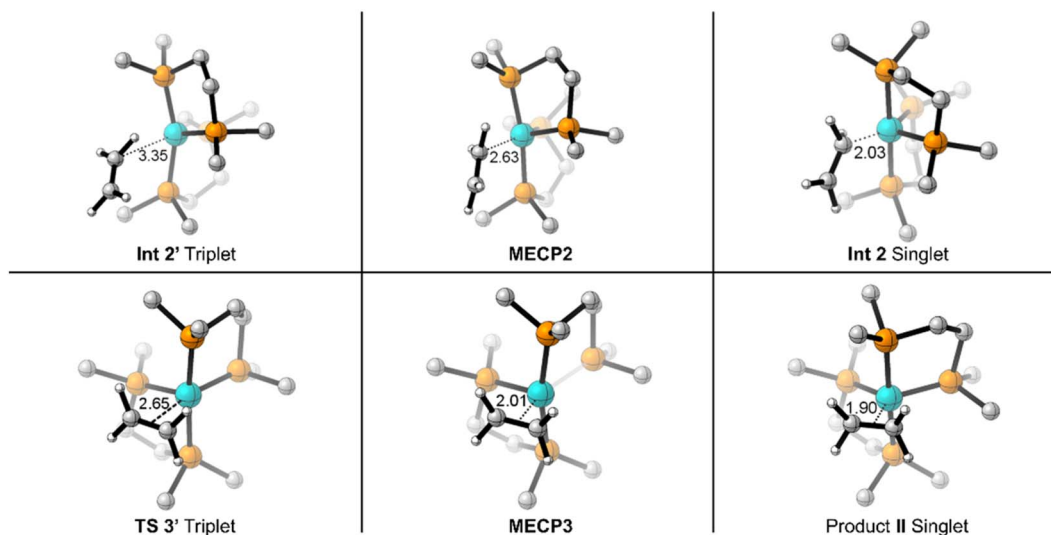

Fig. 3 3D depiction of M06-L optimized geometries for reaction between (DMPE)$_2$Fe and ethylene with key bond/coordination distances (in Å).

Fe-vinyl hydride product **I**. In this series of reaction steps, **MECP2** with an effective bottleneck barrier of 12.0 kcal mol^{-1} relative to triplet **INT 2′** would govern the rate of C–H insertion. For formation of the π-complex product **II**, the lowest energy route involves triplet intermediate **INT 3′** followed by triplet **TS 2′** and then **MECP3**. In this series of reaction steps the triplet **TS 2′** structure governs the rate of forming the π-complex product **II** and has an energy of only 5.4 kcal mol^{-1} relative to triplet **Int 3′**. From a statistical point of view, assuming Curtin–Hammett-type equilibrium of weak coordination structures triplet **INT 2′** and triplet **Int 3′**, the energy difference that controls pathway selectivity is the energy to achieve **MECP2** for C–H insertion and the energy to achieve the triplet **TS 2′** for π-coordination. This energy difference is 7.0 kcal mol^{-1}, and importantly, massively favors forming the π-complex **II**, which is opposite to the experimental 95 : 5 ratio favoring vinyl C–H bond insertion.

Quantitative disagreement with experiment could perhaps be expected given that MECPs only represent an estimate for crossover between singlet and triplet surfaces. Therefore, we estimated the spin–orbit coupling value for **MECP2** using CASPT2(18,11)/ANO-RCC-MB (see ESI†) coupling the lowest energy singlet and triplet states. The energy gap between the singlet and triplet spin states using CASPT2 was calculated to be 2.5 kcal mol^{-1}. Estimation of the spin–orbit coupling value indicates that the energy of **MECP2** would be lowered less than 0.5 kcal mol^{-1} compared to the energy without inclusion of spin–orbit coupling and this does not change the general interpretation of the energy landscapes shown in Fig. 3. Additionally, we also used variational transition state theory (with Polyrate)[25] to re-optimize **TS 2′**. This variational triplet structure has bond distances that are slightly different than **TS 2′**, but the energy is nearly identical. Therefore, this statistical selectivity-based analysis using the singlet and triplet energy surfaces neither provides quantitative nor qualitative agreement with the experimental selectivity.

Dynamics trajectory analysis of reaction pathway selectivity

Because of the disagreement between the energy landscape/statistical analysis and the experimental product ratio, we speculated that the weak σ-coordination and π-coordination intermediates (**INT 2**, **INT 2′**, and **Int 3′**) are likely nonstatistical intermediates, which means there is a lack of significant intermolecular vibrational energy redistribution (IVR) and that these intermediates would either have a very short lifetime or be completely skipped. Moreover, we also speculated that the shapes of the combined singlet and triplet energy surfaces, especially the relatively flat surfaces in the vicinity of the reactive unsaturated triplet and singlet (DMPE)$_2$Fe complex, would provide wandering non-IRC motion during reactive collisions. To test these hypotheses, we performed direct dynamics simulations that can directly account for atomic motion during reactions and identify nonstatistical effects, such as the lack of IVR and non-IRC motion.

Nonstatistical intermediates and non-IRC[26] reaction pathways are now relatively established for some organic reactions.[27–36] However, these types of scenarios are now emerging in organometallic reactions.[37] Most germane, we recently showed that dynamics trajectories were necessary to model the selectivity for the reaction between Cp(PMe$_3$)$_2$Re and ethylene that results in a mixture of Re-vinyl hydride and Cp(PMe$_3$)$_2$Re(η^2-ethylene) products.[38] In this case, trajectories showed that the σ-CH-coordination structure is likely a nonstatistical intermediate and that there are direct pathways for forming the Re-vinyl hydride without σ-coordination or π-coordination. Importantly, the Cp(PMe$_3$)$_2$Re structure and all other structures have a low-spin singlet energy surface. Therefore, a major challenge to address for trajectories involving reactive collision of (DMPE)$_2$Fe with ethylene is the possibility of spin crossover between singlet and triplet spin states.

There are multiple approaches for performing dynamics trajectories that incorporate multiple electronic spin states. Perhaps the most well-known approach is Tully's fewest switches algorithm that provides diabatic surface hopping.[39,40] However, this approach is generally available for hopping between singlet and triplet spin states for photodynamic frameworks. Alternatively, there is the possibility to use an approach based on an adiabatic type of energy surface created through a mixture of spins. Truhlar recently showed that a mixed spin model that incorporates surface coupling provides an approach to obtain energies, forces, and force constants of structures. Therefore, we implemented this mixed spin model into our quasiclassical direct dynamics program Milo.[41,42] This enabled us to execute dynamics trajectories on only singlet and only triplet energy surfaces as well as dynamics trajectories using a mixed spin state surface. Quasiclassical trajectories were initialized by creating a vibrationally-averaged velocity distribution based on normal mode sampling at the experimental temperature of −28 °C, which includes zero-point energy. For transition-state structures, the imaginary frequency was assigned a specific direction to progress and sampled as a positive 10 cm^{-1} normal mode. Each trajectory was propagated using a Verlet integration algorithm with a 0.75 femtosecond (fs) time step. At each step, energies and forces were calculated using UM06-L/6-31G**[LANL2DZ for Fe]. Trajectories were propagated for ~500–1000 fs.

Starting 50 quasiclassical trajectories from **TS 1** with motion in the forwards direction (towards products) on the singlet surface showed only the formation of (DMPE)$_2$-Fe(H)(C$_2$H$_3$) **I**. Formation of this product occurred in less than 50 fs. Trajectories starting from **TS 1** in the reverse (away from products) direction showed initial motion towards the singlet σ-coordination structure **INT 2** but then quickly reverted to the forwards direction in a paddle ball type motion[43] and like the forward direction trajectories only resulted in formation of **I** (see ESI†).

Importantly, these reverse trajectories indicate that the σ-coordination structure **INT 2** is likely a nonstatistical intermediate without a significant lifetime, despite being a fully optimized potential-energy structure. This nonstatistical description is also consistent with **INT 2** having a very shallow potential-energy well and energy almost identical to **TS 1**. This implies that reactive collision trajectories started before the σ-coordination structure will likely breeze through this structure

with direct formation of $(DMPE)_2Fe(H)(C_2H_3)$ **I**. Additionally, this also indicates that the pathway selectivity for C–H insertion *versus* π-coordination likely occurs before C–H bond σ-coordination with the Fe metal center. This prompted us to examine trajectories starting at **MECP2**, which occurs before the σ-coordination structure **INT 2** (see Fig. 2).

MECP2 has ~0.6 Å longer distance between the ethylene and the Fe metal center compared to structure **INT 2**. We propagated 130 trajectories on the singlet spin state surface in the forward direction starting from **MECP2**. Fig. 4a plots these 130 trajectories as the breaking C–H bond length (in the forward direction) in Å *versus* time. When the distance between the distal carbon on ethylene to the Fe center was less than 2.5 Å the trajectory was classified as ending at product **II**. When the distance was close to 3.3 Å then the trajectory was classified as product **I**. This plot shows that within 50 fs nearly all trajectories have fully broken the C–H bond and generated **I**. One of the trajectories recrossed and ended forming **II**. Fig. 4b maps the motion of the 113 reverse direction trajectories by plotting the distance from the distal carbon on ethylene to the Fe center *versus* time. Again, these trajectories propagated on the singlet

surface in the reverse direction resulted in initial dissociation of ethylene followed by rebounding back to collide with the Fe metal center, which is similar motion that occurred in the reverse trajectories starting from **TS 1**. However, unlike the trajectories started from **TS 1**, there was formation of both $(DMPE)_2Fe(H)(C_2H_3)$ **I** and $(DMPE)_2Fe(\eta^2\text{-}C_2H_4)$ **II** structures in this case. The teal-colored trajectories in Fig. 4b end at product **I** and the burgundy-colored trajectories end at **II**. Surprisingly, and likely quantitatively fortuitous, the ratio of **I** : **II** trajectories (108 : 5) is close to the experimental ratio measured by Field. We also initiated and propagated 20 singlet-triplet mixed spin state trajectories starting at **MECP2**. During these trajectories energies and forces are calculated by mixing unrestricted singlet and unrestricted triplet spin states. This provides effective spin crossover if the system changes from a configuration dominated by the triplet spin state to a configuration dominated by the singlet spin state. See the ESI† for further details. The dynamic motion of these mixed spin trajectories was nearly identical to the singlet spin trajectories. However, whenever the triplet spin state dominated the electronic configuration, there was only repulsion between ethylene and Fe center. This triplet
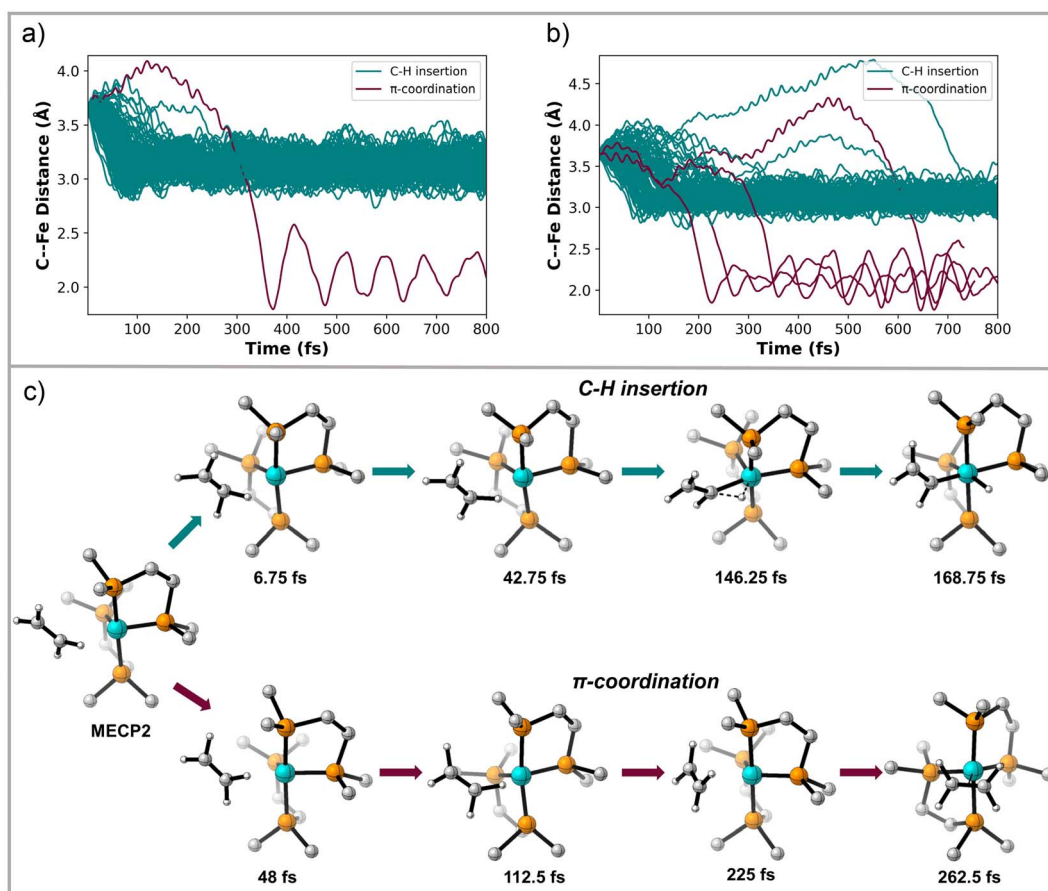

Fig. 4 (a) Plot of Fe−ethylene distance (Å) *versus* time (fs) for singlet surface forward direction trajectories starting from **MECP2**. (b) Plot of Fe−ethylene distance (Å) *versus* time (fs) for reverse direction trajectories starting from **MECP2**. The Fe−ethylene distance was measured from the distal carbon on ethylene to Fe. If the distance between the distal carbon and Fe was <2.5 Å the trajectory was classified as forming product **II**. If this distance was in the vicinity of 3.3 Å it was classified as product **I**. Trajectories plotted in teal color end at the insertion product **I** and trajectories plotted in burgundy end at the π-coordination structure **II**. Note that the y-axis in part b has a slightly different scale than part a. (c) Snapshots of representative C−H insertion and π-coordination trajectories initiated from **MECP2**.

surface repulsion was confirmed with 20 trajectories started from **MECP2** and propagated only on the triplet surface.

We also examined 20 trajectories starting from **MECP3**, and as expected, all singlet spin state trajectories in the forward direction led to the $(DMPE)_2Fe(\eta^2\text{-}C_2H_4)$ **II** structure in about 10 fs. Reverse trajectories resulted in a loosely coordinated structure for only about 5–10 fs followed by return to the metal center to exclusively form structure **II**. No C–H insertion was found from these trajectories. Mixed spin state trajectories starting at **MECP3** resulted in the formation of **II** for both propagation in the forwards and backwards directions because this crossing point occurs after transition state on the triplet surface (see Fig. 2).

Because of the reaction pathway branching that occurred in the reverse and rebound trajectories starting at **MECP2** we decided to sample the reaction landscape using metadynamics simulations, which provided alternative starting points for reactive collision trajectories. Specifically, the metadynamics simulations provided a straightforward way of identifying starting structures before **MECP2**. Metadynamics simulations were performed using GTH-PBE[44]/DZVP-MOLOPT-SR-GTH[45] in CP2K 7.1.[46] Fig. 5a shows the singlet spin state metadynamics simulation energy surface that connects structures **I** to **II** using collective variables (CVs) that describe both C–H bond formation/cleavage and ethylene coordination/dissociation (see ESI† for CV descriptions). Fig. 5b shows structures **A, B,** and **C**

that correspond to metadynamics structures with Fe–C distances of 2.5, 2.7, and 2.9 Å. Because the metadynamics simulations served only to identify general structures before MECP2, structures **A, B,** and **C** were then constrained with their CV values and then reoptimized with UM06-L/6-31G** [LANL2DZ] in preparation for trajectories. Structures **A** and **B** have a slightly lower singlet energy while structure **C** has a slightly lower triplet energy.

Because structure **C** has a lower energy triplet spin state, we launched mixed spin state trajectories with the expectation that reactive collisions would occur with crossover from a triplet spin dominated structure to a singlet spin dominated structure. However, the mixed spin state trajectories resulted in repulsive collision between ethylene and the Fe metal center and no formation of either **I** or **II**. Additionally, none of these mixed spin state trajectories showed a significant increase in singlet spin-state character. The trajectories remained dominated by the triplet spin configuration, and after the collision, there was repulsion between ethylene and $(DMPE)_2Fe$, which would be anticipated by inspection of the triplet surface that is overall repulsive. In retrospect the results of the trajectories starting from structure **C** are perhaps not surprising since the MECPs are several kcal mol^{-1} higher in energy. This scenario is akin to trajectories starting at reactant-like structures with reactant energy, which has low probability of overcoming a barrier. To test this theory, we started trajectories from **C** with up to
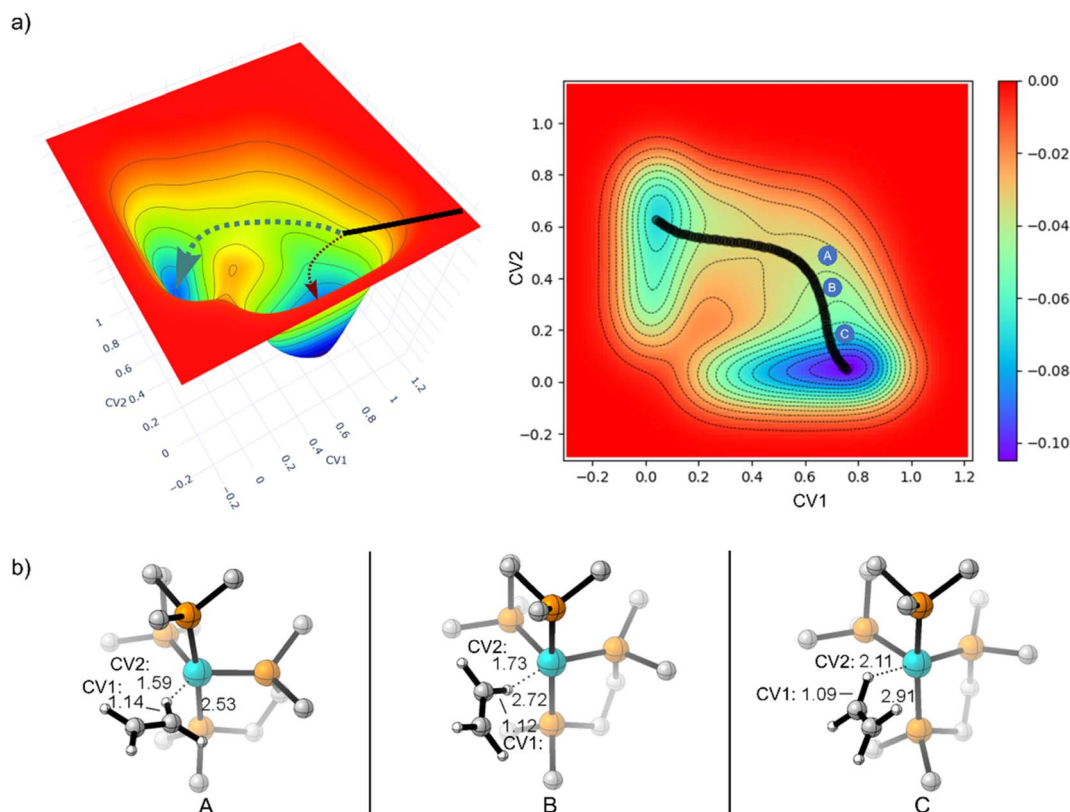

Fig. 5 (a) 3D plot of PBE metadynamics singlet spin state surface. Collective variable 1 (x-axis) is the C−H distance. Collective variable 2 (y-axis) is the Fe−H distance. (b) 3-dimensional representations of structures A, B, and C after constrained optimization of CV with UM06-L.

20 kcal mol^{-1} of additional center of mass translational velocity for ethylene, which would provide enough energy to overcome the MECP bottleneck. Indeed, in these 10 mixed spin state trajectories (see ESI†) with extra translational energy there was crossover from a triplet spin dominated structure to a singlet spin dominated structure, but surprisingly there was only formation of the π-coordination structure **II**. This suggests that in these trajectories C–H insertion did not occur because the additionally translational energy induced ultrafast collision between ethylene and the Fe center before the added energy could redistribute to the C–H vibrational modes, which is required for C–H bond cleavage.

In contrast to starting at structure **C**, the mixed spin state trajectories started from structures **A** and **B** showed formation of **I** and **II**, but only from trajectories that were generally had a singlet ground state. This provided the impetus to perform

adiabatic singlet spin state surface dynamics for the remainder of the trajectories. Fig. 6a plots 91 singlet spin state reactive collision trajectories sampled and propagated starting from structure **A**. The teal lines represent trajectories that ended in product **I** and the burgundy lines represent trajectories that ended at product **II**. In this set of trajectories, there was a nearly 69 : 22 ratio of **I** : **II** (Fig. 6a). Fig. 6b plots 100 singlet spin state reactive collision trajectories sampled and propagated starting from structure **B**. Again, the teal lines represent trajectories that ended in product **I** and the burgundy lines represent trajectories that ended at product **II**. For the **B** set of trajectories there was a nearly 77 : 23 ratio for forming **I** : **II**.

Inspection of the plotted trajectories in Fig. 6 reveals that **I** and **II** are generally formed in 100–200 fs from the start of the trajectory, although there are few trajectories that lag up to about 400 fs to form a product. This relatively short time between the start of the trajectory and product formation confirms that the weak σ-complex **INT 2** should probably best be viewed as a nonstatistical intermediate with a very shallow energy well that is likely skipped or bypassed in most trajectories. This viewpoint is consistent with the metadynamics generated energy landscape that shows a relatively flat energy surface when ethylene only weakly interacts with the Fe metal center and suggests that the initial collisional orientation between ethylene and (DMPE)$_2$Fe determines the reaction pathway. On the singlet energy surface (and the mixed spin surface) the pathway towards the insertion product **I** is probably best viewed as the dynamically direct pathway while the π-coordination product is the off-pathway (non-IRC type) product, which is illustrated by the dotted trajectory arrows in Fig. 5a. This preference occurs regardless of the starting ethylene position and is surprising because the Fe-vinyl hydride product is thermodynamically less stable than the π-coordination product. However, it is important to realize that entry into the π-coordination pathway is more restricted since it is only favorable when the Fe d-orbitals (occupied and vacant) are properly aligned with the ethylene π and π* orbitals.[47] This restriction will naturally provide kinetic selectivity in a reaction where dynamic nonstatistical motion controls selectivity.

Fig. 6 (a) Plot of adiabatic singlet spin state trajectories beginning at structure **A** and moving in the direction towards forming product. Teal lines represent trajectories that end at product **I**. Burgundy lines represent trajectories that end at product **II**. The vertical axis is the distal carbon on ethylene to Fe distance and the horizontal axis is trajectory time (fs). (b) Plot of adiabatic singlet spin state trajectories beginning at structure **B** and moving in the direction towards forming product. Teal lines represent trajectories that end at product **I**. Burgundy lines represent trajectories that end at product **II**. The vertical axis is the distal carbon on ethylene to Fe distance and the horizontal axis is trajectory time (fs). If the distance between the distal carbon and Fe was <2.5 Å the trajectory was classified as forming product **II**. If this distance was in the vicinity of 3.3 Å it was classified as product **I**.

Conclusions

DFT optimized singlet and triplet spin state energy landscapes with transition-state structures and MECP structures provides an incorrect interpretation of pathway selectivity for the spin crossover reaction between ethylene and (DMPE)$_2$Fe. Using both single spin state and mixed singlet/triplet spin state quasiclassical DFT-based direct dynamics trajectories we showed that there are direct dynamic pathways leading to both the vinyl insertion product (DMPE)$_2$Fe(H)(C$_2$H$_3$) **I** and **II** with an inherent preference for **I**. The trajectory results are qualitatively and quantitatively consistent with the experimental kinetic ratio of products. Overall, this work demonstrates the need to consider evaluating dynamics trajectories in spin crossover reactions to determine the origin of reaction pathway selectivity, especially for highly reactive, coordinatively unsaturated metal complexes.
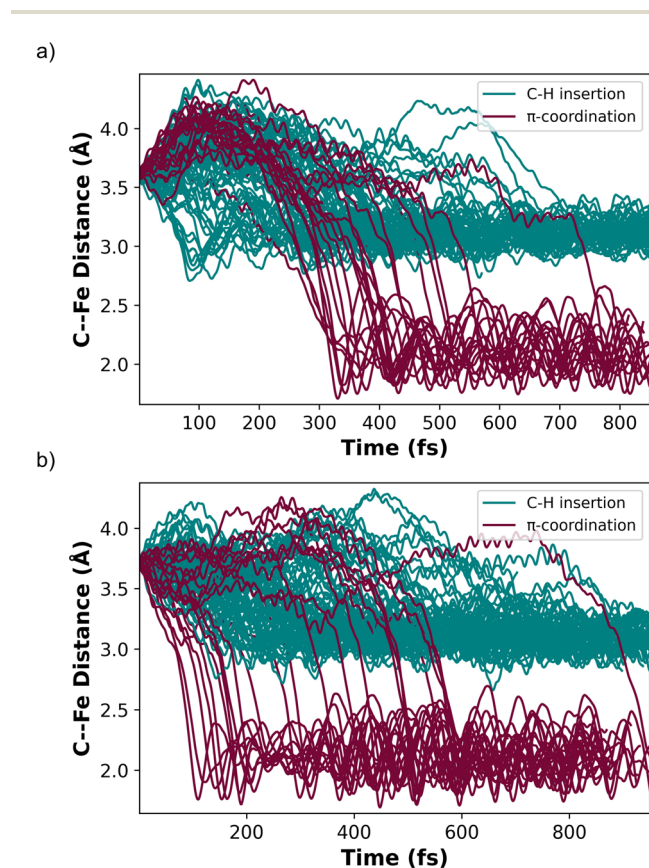
Data availability

Computational details to replicate the data in this work can be found in the ESI†. The Milo direct dynamics program that can be used to replicate trajectories can be found on GitHub at: **https://github.com/DanielEss-lab/milo**.

Author contributions

D. Ess designed calculations. M. Davenport carried out calculations. M. Davenport, J. Kirkland, and D. Ess analyzed results and wrote the manuscript.

Conflicts of interest

There are no conflicts to declare.

Acknowledgements

Notes and references

1 H. Eyring, *J. Chem. Phys.*, 1935, **3**, 107–115.
2 K. J. Laidler and M. C. King, *J. Phys. Chem.*, 1983, **87**, 2657–2664.
3 D. G. Truhlar, B. C. Garrett and S. J. Klippenstein, *J. Phys. Chem.*, 1996, **100**, 12771–12800.
4 R. Poli, *Chem. Rev.*, 1996, **96**, 2135–2204.
5 D. Schröder, S. Shaik and H. Schwarz, *Acc. Chem. Res.*, 2000, **33**, 139–145.
6 J. N. Harvey, M. Aschi, H. Schwarz and W. Koch, *Theor. Chem. Acc.*, 1998, **99**, 95–99.
7 M. V. Baker and L. D. Field, *J. Am. Chem. Soc.*, 1986, **108**, 7436–7438.
8 M. V. Baker and L. D. Field, *J. Am. Chem. Soc.*, 1986, **108**, 7433–7434.
9 P. O. Stoutland and R. G. Bergman, *J. Am. Chem. Soc.*, 1985, **107**, 4581–4582.
10 K. M. Smith, R. Poli and J. N. Harvey, *Chem.–Eur. J.*, 2001, **7**, 1679–1690.
11 D. H. Ess, *Acc. Chem. Res.*, 2021, **54**, 4410–4422.
12 M. Paranjothy, R. Sun, Y. Zhuang and W. L. Hase, *Wiley Interdiscip. Rev.: Comput. Mol. Sci.*, 2013, **3**, 296–316.
13 B. K. Carpenter, *Annu. Rev. Phys. Chem.*, 2005, **56**, 57–89.
14 B. K. Carpenter, *Chem. Rev.*, 2013, **113**, 7265–7286.
15 U. Lourderaj, K. Park and W. L. Hase, *Int. Rev. Phys. Chem.*, 2008, **27**, 361–403.
16 X. Ma and W. L. Hase, *Philos. Trans. R. Soc., A*, 2017, **375**, 20160204.
17 R. Ditchfield, W. J. Hehre and J. A. Pople, *J. Chem. Phys.*, 1971, **54**, 724–728.
18 M. J. Frisch, G. W. Trucks, H. B. Schlegel, G. E. Scuseria, M. A. Robb, J. R. Cheeseman, G. Scalmani, V. Barone, G. A. Petersson, H. Nakatsuji, X. Li, M. Caricato, A. V. Marenich, J. Bloino, B. G. Janesko, R. Gomperts, B. Mennucci, H. P. Hratchian, J. V. Ortiz, A. F. Izmaylov, J. L. Sonnenberg, D. Williams-Young, F. Ding, F. Lipparini, F. Egidi, J. Goings, B. Peng, A. Petrone, T. Henderson, D. Ranasinghe, V. G. Zakrzewski, J. Gao, N. Rega, G. Zheng, W. Liang, M. Hada, M. Ehara, K. Toyota, R. Fukuda, J. Hasegawa, M. Ishida, T. Nakajima, Y. Honda, O. Kitao, H. Nakai, T. Vreven, K. Throssell, J. A. Montgomery Jr, J. E. Peralta, F. Ogliaro, M. J. Bearpark, J. J. Heyd, E. N. Brothers, K. N. Kudin, V. N. Staroverov, T. A. Keith, R. Kobayashi, J. Normand, K. Raghavachari, A. P. Rendell, J. C. Burant, S. S. Iyengar, J. Tomasi, M. Cossi, J. M. Millam, M. Klene, C. Adamo, R. Cammi, J. W. Ochterski, R. L. Martin, K. Morokuma, O. Farkas, J. B. Foresman and D. J. Fox, *Gaussian 16, Revision B.01*, Gaussian Inc., Wallingford, CT, 2016.
19 F. Weigend and R. Ahlrichs, *Phys. Chem. Chem. Phys.*, 2005, **7**, 3297–3305.
20 Y. Zhao and D. G. Truhlar, *J. Chem. Phys.*, 2006, **125**, 194101.
21 D.-H. Kwon, B. L. Small, O. L. Sydora, S. M. Bischof and D. H. Ess, *J. Phys. Chem. C*, 2019, **123**, 3727–3739.
22 W. Lee, J. Zhou and O. Gutierrez, *J. Am. Chem. Soc.*, 2017, **139**, 16126–16133.
23 A. V. Marenich, C. J. Cramer and D. G. Truhlar, *J. Phys. Chem. B*, 2009, **113**, 6378–6396.
24 L.-A. H. J. D. Snyder, K. E. Faleumu, A. R. Schultz and D. H. Ess, *MECPro Version 1.0.6*, Minimum Energy Crossing Program, 2020.
25 J. Zheng, J. L. Bao, R. Meana-Pañeda, S. Zhang, B. J. Lynch, J. C. Corchado, Y.-Y. Chuang, P. L. Fast, W.-P. Hu, Y.-P. Liu, G. C. Lynch, K. A. Nguyen, C. F. Jackels, A. Fernandez Ramos, B. A. Ellingson, V. S. Melissas, J. Villà, I. Rossi, E. L. Coitiño, J. Pu, T. V. Albu, A. Ratkiewicz, R. Steckler, B. C. Garrett, A. D. Isaacson and D. G. Truhlar, *Polyrate-version 2017-C*, University of Minnesota, Minneapolis, MN, 2017.
26 K. Fukui, *Acc. Chem. Res.*, 1981, **14**, 363–368.
27 T. Bekele, C. F. Christian, M. A. Lipton and D. A. Singleton, *J. Am. Chem. Soc.*, 2005, **127**, 9216–9223.
28 B. Biswas and D. A. Singleton, *J. Am. Chem. Soc.*, 2015, **137**, 14244–14247.
29 B. K. Carpenter, *J. Am. Chem. Soc.*, 1995, **117**, 6336–6344.
30 Z. Chen, Y. Nieves-Quinones, J. R. Waas and D. A. Singleton, *J. Am. Chem. Soc.*, 2014, **136**, 13122–13125.
31 C. Doubleday, G. Li and W. L. Hase, *Phys. Chem. Chem. Phys.*, 2002, **4**, 304–312.
32 C. Doubleday, C. P. Suhrada and K. N. Houk, *J. Am. Chem. Soc.*, 2006, **128**, 90–94.
33 S. R. Hare, A. Li and D. J. Tantillo, *Chem. Sci.*, 2018, **9**, 8937–8945.
34 S. R. Hare and D. J. Tantillo, *Pure Appl. Chem.*, 2017, **89**, 679–698.

35 J. G. López, G. Vayner, U. Lourderaj, S. V. Addepalli, S. Kato, W. A. deJong, T. L. Windus and W. L. Hase, *J. Am. Chem. Soc.*, 2007, **129**, 9976–9985.

36 B. R. Ussing, C. Hang and D. A. Singleton, *J. Am. Chem. Soc.*, 2006, **128**, 7594–7607.

37 S. R. Hare and D. J. Tantillo, *Chem. Sci.*, 2017, **8**, 1442–1449.

38 B. Yang, A. Schouten and D. H. Ess, *J. Am. Chem. Soc.*, 2021, **143**, 8367–8374.

39 J. E. Subotnik, *J. Phys. Chem. A*, 2011, **115**, 12083–12096.

40 J. C. Tully, *J. Chem. Phys.*, 1990, **93**, 1061–1071.

41 M. S. Teynor, N. Wohlgemuth, L. Carlson, J. Huang, S. L. Pugh, B. O. Grant, R. S. Hamilton, R. Carlsen and D. H. Ess, *Milo, Revision 1.0.1*, Brigham Young University, Provo UT, 2022.

42 B. Yang, L. Gagliardi and D. G. Truhlar, *Phys. Chem. Chem. Phys.*, 2018, **20**, 4129–4136.

43 R. Carlsen, J. R. Jenkins, T.-C. J. Huang, S. L. Pugh and D. H. Ess, *Organometallics*, 2019, **38**, 2280–2287.

44 J. P. Perdew, K. Burke and M. Ernzerhof, *Phys. Rev. Lett.*, 1997, **78**, 1396.

45 J. VandeVondele and J. Hutter, *J. Chem. Phys.*, 2007, **127**, 114105.

46 T. D. Kühne, M. Iannuzzi, M. D. Ben, V. V. Rybkin, P. Seewald, F. Stein, T. Laino, R. Z. Khaliullin, O. Schütt, F. Schiffmann, D. Golze, J. Wilhelm, S. Chulkov, M. H. Bani-Hashemian, V. Weber, U. Borštnik, M. Taillefumier, A. S. Jakobovits, A. Lazzaro, H. Pabst, T. Müller, R. Schade, M. Guidon, S. Andermatt, N. Holmberg, G. K. Schenter, A. Hehn, A. Bussy, F. Belleflamme, G. Tabacchi, A. Glöß, M. Lass, I. Bethune, C. J. Mundy, C. Plessl, M. Watkins, J. VandeVondele, M. Krack and J. Hutter, *J. Chem. Phys.*, 2020, **152**, 194103.

47 J. Silvestre, M. J. Calhorda, R. Hoffmann, P. O. Stoutland and R. G. Bergman, *Organometallics*, 1986, **5**, 1841–1851.